Resolving microscale surface temperature variability during a heatwave using a dense sensor network

Mark T. Ireland[1]*, Hector G. Barnett[1], Abdullah Kahraman[2,3] and Charles K. Dunham[1]

[1]School of Natural and Environmental Science, Newcastle University
[2]School of Engineering, Newcastle University, Newcastle upon Tyne, UK
[3]Tyndall Centre for Climate Change Research, Newcastle University, Newcastle upon Tyne, UK

*Corresponding author: mark.ireland@newcastle.ac.uk

Abstract

High-resolution observations of near-surface temperature variability are essential for understanding heat exposure during extreme weather events, yet are rarely available from dense, regularly spaced in situ measurement grids, with most existing observations derived from unevenly distributed sensor networks. Here, we analyse temperature measurements derived from a dense network of over 3,000 nodal seismometers deployed across a 6 km^2 area in North Yorkshire, UK, during the July 2022 heatwave, using data from embedded microcontroller sensors. Although the embedded microcontroller sensors provide incidental environmental measurements at unprecedented spatial and temporal resolution, with over 80 million logged temperatures recorded at 100 s intervals for 34 days.

Microcontroller derived temperature measurements were statistically corrected using co-located meteorological observations to account for systematic biases introduced by the thermal response of the sensor housing to closer approximate true near-surface temperatures across the network. The corrected dataset reveals strong spatial heterogeneity in surface temperatures, with mean differences of up to 3.6 °C at distances of 100–200 m and extreme contrasts exceeding 17 °C during peak heating conditions. Spatial variability is interpreted to be strongly modulated by meteorological forcing, with daytime heatwave conditions exhibiting the greatest heterogeneity, while nighttime periods show substantial homogenisation. Systematic but modest differences are observed between land-use classes (~0.1 °C), expressed primarily through variations in persistence and extremes rather than mean temperature alone.

The results highlight the importance of sub-kilometre variability in near surface temperature fields and demonstrate the potential of repurposing incidental environmental sensing to characterise microclimate environments at scales relevant to ecosystem dynamics and human exposure. More broadly, the findings open the potential, with improved calibration, that dense geophysical arrays could provide unique insights into fine-scale meteorological dynamics with implications for the interpretation of satellite-derived land surface temperature, the development of high-resolution modelling approaches, and the assessment of heat-related risks.

1 Introduction

Spatial and temporal variations in both air and land surface temperature have implications for Earth systems, including climate systems (e.g. Betts et al., 1996), biogeochemical cycles (e.g. Burke et al., 2003) and the interaction with the built environment (e.g. Nuruzzaman, 2015). It is widely documented that land use and the built environment impact air and surface temperatures within the Earth system (Tran et al., 2017), and specifically, in the context of urban areas that built up areas are known to exert a significant influence on their local climate, and are generally warmer than their surroundings (e.g. Kershaw et al., 2010). While modelling approaches are widely used to investigate microclimates, understanding fine-scale variability requires high-resolution field observations (Yang et al., 2013). Such measurements provide direct evidence of microclimate processes and are essential for quantifying their impacts. This is particularly important in ecological contexts, where fine-scale thermal variability influences habitat conditions (Kemppinen et al., 2024) and for human health, where local temperature extremes affect heat exposure and associated risks (Schinasi et al., 2018).

The heterogeneity of surface temperature affects the surface energy and water budgets, as well as the land-atmosphere exchanges of momentum, heat, water and other constituents (Giorgi & Avissar, 1997). Land surface temperature (LST) derived from satellite thermal infrared observations provides valuable spatial coverage at moderate resolution, ranging from 1 km for MODIS (Hulley & Hook, 2017) down to 70 m for ECOSTRESS (Earth Science Data Systems, 2025); however, their relatively low temporal frequency and sensitivity to cloud contamination limit their ability to fully resolve short-term and fine-scale thermal variability in urban environments (Huang et al., 2013). This often leads to a low temporal resolution or intermittent temporal coverage. To resolve this lack of data at the finer scale, the use of modelling is commonplace (e.g. de La Flor & Domınguez, 2004), however this is reliant on calibration data. Recently there have been efforts to accurately estimate air temperature with low-cost devices (Maclean et al., 2021), however the dedicated development and deployment of high density and spatially extensive sensor networks remains logistically challenging, particular in terms of operation, maintenance and data retrieval. As such there is a lack of case studies that use in situ measurements to reveal the fine scale spatial variability in land surface temperature.

Many sensor systems and electronic devices record environmental variables, such as chip temperature, as a secondary function of their routine operation. These measurements can potentially enable incidental environmental sensing, although there are limited studies examining temperatures from devices to investigate environmental processes (e.g. Arachchige et al., 2023). Here, temperature measurements that were recorded principally for instrument health and performance are repurposed to investigate near-surface thermal variability.

We investigate the spatial and temporal variations in near-surface temperature within a mixed land use setting during the July 2022 heatwave in northwest Europe. During this event, a new UK record daily maximum temperature of 40.3 °C was recorded on 19 July, representing the most extreme heatwave conditions seen in the instrumental record (Yule et al., 2023). The study utilises temperature measurements acquired from microcontroller-based sensors embedded within seismic nodes deployed during a geophysical survey at RAF Leeming, North Yorkshire, UK in July 2022 (**Figure 1**). Although the survey was not designed for environmental monitoring, the high spatial density and extent of the array provide a unique opportunity to resolve near-surface temperature variability at microscales during a period of extreme heat.

The resulting dataset, covering approximately 6 km^2, represents one of the densest in situ measurements of near-surface temperature reported to date. These data are used to characterise spatial and temporal temperature variability and are evaluated against observations from a co-located meteorological station. The results provide insight into fine-scale thermal variability across a mixed land-use environment under extreme heatwave conditions.

2 Data and Methodology

2.1 Data acquisition and experimental design

Temperature measurements were obtained from microcontroller sensors embedded within the STRYDE seismic nodes deployed as part of a geophysical survey in North Yorkshire, UK (**Figure 1**). A total of 3,218 seismic nodes were distributed across an approximately 6 km^2 area between 7 July and 5 August 2022. Temperature data from 3,083 were used in this study, with the remaining nodes excluded due to incomplete records arising from issues relating to deployment and retrieval or damage. The deployment geometry comprised 25 lines, predominantly oriented east–west and spaced at 100 m intervals, with nodes positioned at 10 m spacing along each line. One line followed an access road to the site and was oriented approximately north–south.

The seismic nodes were deployed using a hand auger to embed the device into the ground so that the top of the device was nearly flush with the surface. In all cases devices were only deployed on unbuilt ground (grass or soil) and the lowest part of the device was located at a maximum of 10 cm depth. The position of the microcontroller within the device is such that it was positioned approximately 5 cm beneath surface. Each device logged temperature at 100 s intervals, with a nominal precision of ±1 °C and integer output. The resulting dataset comprises more than 80 million individual recorded temperatures. Throughout this study these temperatures are referred to as *raw sensor temperatures*.

Figure 1. Location of the dense seismic array deployed at RAF Leeming, North Yorkshire, UK. (a) Location of 3,083 seismic nodes across the study area overlaid on aerial imagery (sourced from ESRI). The weather station used for calibration and comparison is indicated by the white star, while the red rectangle denotes the area shown in panel (b). (b) Detailed view of the sensor array surrounding the weather station, including the three calibration sensors (red symbols) used to develop the temperature bias-correction model. (c) Location of the study area within the United Kingdom. Coordinates are shown in the British National Grid

The internal temperature sensor is integrated within an STM32L431 microcontroller. The sensor generates a temperature-dependent voltage that is digitized through the on-chip ADC and converted to temperature using factory calibration constants. Because the

sensor measures microcontroller die temperature, recorded values could reflect both environmental temperature and internal self-heating. To assess the latter, diagnostic metadata describing node operation were extracted from three calibration nodes and compared with measured temperatures. Metadata describing signal, timing, and data-quality characteristics were extracted from the SEG-D headers of the three nodes used in the temperature correction workflow. Pearson correlation coefficients were then calculated between each metric and internal node temperature.

A permanent Met Office ground-based weather station located within the deployment array provided reference meteorological observations, including near-surface and grass temperature, enabling calibration and validation of sensor-derived measurements. The Met Office station data is available from CEDA hosted Met Office Integrated Data Archive System (MIDAS) (Met Office, 2012). Heatwave periods were identified following the Met Office definition ('What is a heatwave?', n.d.) as periods of at least three consecutive days with daily maximum air temperature exceeding 25 °C, the threshold applicable to North Yorkshire. Throughout this study these temperatures are referred to as *weather station temperatures*. The UK Hadley Centre Central England Temperature (HadCET) dataset provides the daily temperatures to describe the wider meteorological conditions across the British Isles during the heatwave.

2.2 Reference Temperature Correlation

The raw sensor temperatures have been used here opportunistically as they were logged as metadata throughout the duration of the geophysical surveying. Because the temperature measurements were recorded as part of routine instrument operation rather than for environmental monitoring, no dedicated pre-deployment temperature calibration was undertaken beyond the manufacturer's factory calibration. Comparison with co-located weather station measurements shows that the sensor data exhibit systematic bias relative to the grass reference temperature (**Figure 2**), which cannot be explained by spatial separation which is <30m for the nearest device. This bias is primarily associated with differences between the temperature measured by the seismic node and the ambient environmental temperature. The node records temperature using an internally calibrated microcontroller sensor located within the device enclosure rather than a dedicated meteorological temperature sensor. Consequently, the recorded temperatures are influenced by the thermal environment within the housing, including shielding from direct radiative forcing and modest differences in the timing and magnitude of the measured diurnal temperature cycle relative to standard meteorological observations. To account for these biases, a systematic evaluation of the raw sensor temperature data and co-located weather station observations was undertaken.

Although raw sensor temperatures exhibit a slightly stronger correlation with air temperature than with grass temperature ($R^2 \approx 0.40$ vs 0.33), the bias relative to air temperature is weakly structured with respect to time and therefore less reliably modelled ($R^2 \approx 0.1–0.2$). In contrast, bias relative to grass temperature exhibits strong diurnal structure and can be effectively modelled using a statistical approach ($R^2 \approx 0.8$) (**Figure 2**). Consequently, correction relative to grass temperature yields a substantially greater reduction in error and is therefore adopted.

Variance decomposition further supports this distinction, indicating that approximately 70% of the variance in bias relative to grass temperature is explained by diurnal structure, whereas only ~10% of the variance in bias relative to air temperature is structured, with the remainder dominated by within-hour variability.

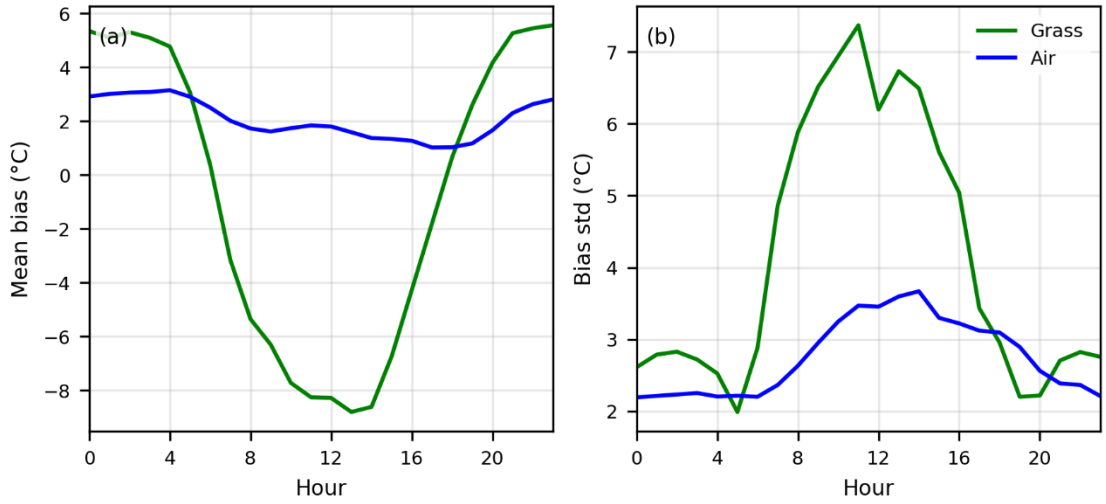

Figure 2. Diurnal variation in bias relative to grass and air temperature. Bias relative to grass temperature exhibits a clear diurnal structure, whereas bias relative to air temperature shows weak temporal organisation.

Throughout this study, the corrected temperatures are interpreted as near-surface environmental temperatures that most closely approximate grass temperature rather than standard 2 m air temperature or remotely sensed land surface temperature.

2.3 Data preprocessing

Raw sensor temperature time series were first collated and associated with spatial metadata (location and elevation). To reduce the influence of probable anomalous measurements, a spatial consistency filter was applied. For each sensor, the nearest sensor was identified, and observations were removed where the absolute difference between paired raw sensor temperatures exceeded a 5°C threshold. This step exploits the high spatial density of the array to identify physically improbable deviations.

To reduce high-frequency noise and sensor-specific variability, each time series was smoothed using a Gaussian kernel filter. For each observation, a weighted average of neighbouring values within a temporal window (±3 bandwidths) was computed, with weights defined by a Gaussian function of temporal distance. The bandwidth parameter controls the degree of smoothing and defines the effective temporal scale of the filter. The smoothed time series were subsequently resampled to regular hourly intervals by averaging all observations within each interval. This ensured temporal alignment across all sensors and with Met Office meteorological datasets.

Additional variables were derived to support subsequent analysis and calibration. Sensor locations were used to calculate the distance to the reference weather station, providing a measure of separation from calibration source. Each observation was also classified as daytime or nighttime based on solar position, calculated from location and timestamp. This enables differentiation of diurnal effects in sensor behaviour.

All datasets, including sensor measurements and weather station observations, were standardised to a common hourly resolution and a continuous time index was constructed over the study period with all datasets were merged onto this index.

2.4 Bias adjustment of sensor temperatures

A subset of three sensors, located <50m from the Met Office station, were chosen based on the consistency of their temperature records relative to the neighbouring sensors for the bias correction. The permanent ground-based weather station located within the study area provided reference meteorological observations, including grass temperature, humidity, wind speed and incoming radiation. These data were temporally aligned with the sensor measurements and used as the reference dataset for calibration and evaluation.

Using these sensors, four different regression models were trained to predict the bias between the microcontroller temperature and the reference grass temperature initially as a function of: i) smoothed sensor temperature; ii) distance to the weather station; iii) sensor elevation and iv) cyclic representations of time (sine and cosine transforms of hour of day). Separate tests of humidity, wind speed and incoming radiation were evaluated as predictor variables. The four regression models tested were: Random Forest, Extra Trees, Gradient Boosting, and Histogram Gradient Boosting. These represent two classes of tree-based methods: bagging approaches, which reduce variance through averaging (Random Forest, Extra Trees), and boosting approaches, which iteratively improve predictions by correcting residual errors (Gradient Boosting, Histogram Gradient Boosting) (James et al., 2023). All models were trained using the same feature set and training dataset and evaluated using consistent performance metrics. After preprocessing and filtering, 1,913 hourly observations were retained, of

which 80% were used for training and 20% for testing. Model performance is reported on the held-out test set.

The regression models were employed to capture non-linear relationships between predictors and reference temperature. All models were implemented using the scikit-learn Python library (Pedregosa et al., 2011). Model-specific hyperparameters were either tuned using cross-validation (for Gradient Boosting) or set to regularised values. Bias predictions were constrained using percentile-based filtering applied on an hourly basis to limit extreme values while preserving diurnal variability. Model performance was evaluated using standard metrics, including root mean squared error (RMSE) and coefficient of determination (R^2), mean absolute error (MAE) and mean bias error (MBE). The trained models were subsequently applied to all raw sensor temperatures in the array to generate corrected sensor temperature estimates, thereby accounting for systematic bias and improving comparability with reference measurements. The parameters for each model can be found in the Supplementary Material 1. Throughout this study these temperatures are referred to as *corrected sensor temperatures*.

2.5 Spatial processing and interpolation

Spatial structure in the temperature field was quantified using semi-variograms calculated independently for each hourly time step. For each hourly timestamp, pairwise distances between all sensor locations were computed in projected coordinates, and the semi-variance was evaluated as half the squared difference in temperature between sensor pairs. Semi-variances were grouped into discrete lag bins (20 m width) up to a maximum separation distance of 800 m and mean semi-variance values were calculated for each bin, with bins containing fewer than 50 pairs excluded to reduce statistical noise. From each variogram, the nugget was defined as the semi-variance at the smallest lag, the sill as the mean semi-variance of the upper 20% of lag distances, and the range as the distance at which the semi-variance reached 95% of the sill. This was repeated for all time steps (n = 687), enabling temporal analysis of spatial correlation length scales. Summary statistics of the variogram parameters were then used to characterise the typical spatial structure of the temperature field and to inform subsequent interpolation, with the median range providing a constraint on the spatial scale of correlation.

The high spatial density of the array enables detailed mapping of near-surface temperature variability. To generate continuous temperature fields, point measurements were interpolated using inverse distance weighting (IDW). This method assigns weights to observations based on distance, preserving local variability and exploiting the relatively uniform sensor spacing. Interpolation was performed independently for each time interval. The resulting gridded datasets enable interpretation of spatial temperature patterns at sub-kilometre scales, exceeding the resolution of commonly available satellite-derived land surface temperature products. Spatial and temporal variability in

temperature were analysed using a combination of statistical techniques. Spatial clustering was assessed using metrics such as Moran's I, while gradients in temperature were evaluated using first-order spatial derivatives. Temporal periodicity was examined using Fourier-based spectral analysis.

3 Results

3.1 Meteorological Conditions

3.1.1 July 2022 heatwave

In July 2022, the UK exceeded 40 °C for the first time in the instrumental record, with the previous national maximum of 38.7 °C surpassed at 46 stations across England from south to north. The UK mean daily maximum temperature also exceeded 30 °C for the first time, and 18–19 July became the hottest days recorded (Figure 3). According to the Met Office, a heatwave is defined as at least three consecutive days with daily maximum temperature meeting or exceeding a location-specific threshold (Met Office, n.d.). These county-level thresholds range from 25 to 28 °C and are based on the 1991–2020 climatology of daily maximum temperature at the midpoint of meteorological summer. The event developed as a high-pressure system moved across the UK during 16–17 July, allowing temperatures to rise progressively from the mid-20s to the low 30s °C across much of England and Wales. As the high shifted eastwards, exceptionally hot continental air was advected northwards, producing a synoptic configuration highly favourable for extreme heat across parts of the UK.

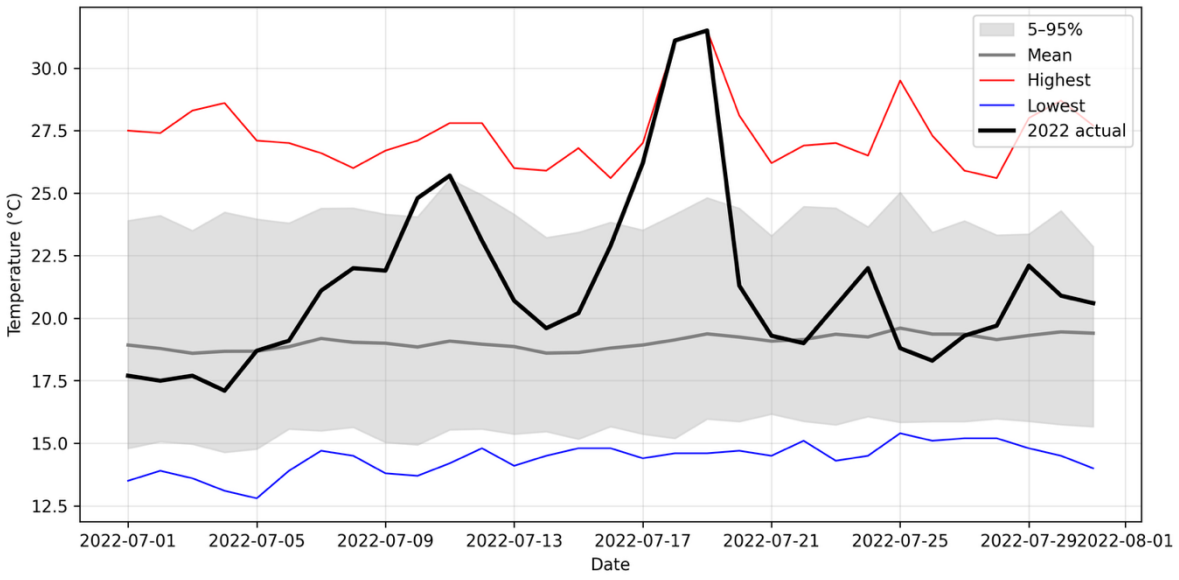

Figure 3. UK maximum temperature during 2022 July (thick black line) and the historical context. 1991-2020 is used as the base period.

From 1878 to 2022, both the number of days exceeding the 90th percentile in temperature and the occurrence of heat waves have increased (Yule et al., 2023) . Remarkably, between 1994 and 2022, 79% of years experienced at least one summer heat wave, more than any earlier 29-year period, reflecting a steady rise in monthly average temperatures (Yule et al., 2023). According to a recent model-based study, experiencing a day over 40 °C is currently a 1-in-24 year event, though this probability is rising quickly (Kay et al., 2025) . Additionally, the UK's hottest summer days have warmed at a rate more than three times faster than global averages over the past century (Hawkins et al., n.d.).

The heatwave exerted significant effects across various sectors. It contributed to widespread fires in London and other regions (John & Rein, 2025) , with a six-fold increase in the probability of very high fire danger projected due to warming trends (Burton et al., 2025) . In London alone, 370 out of 1,773 fatalities have been attributed to the heatwave (Simpson et al., 2024). There were also effects on public health and overall well-being (e.g. Savu, 2025). Additionally, the event impacted transportation, energy supply, education (Howarth et al., 2024), and food systems (Davie et al., 2023).

3.1.2 Observations at the site

While air temperature is conventionally recorded at an elevation of 2 m to meet standard meteorological requirements, surface and soil temperatures diverge from these readings and are influenced by the distinct properties of soil, vegetation, and built environments.

The Met Office weather station located at RAF Leeming recorded a maximum grass temperature of 51.6ºC at 2022-07-18 11:30:00 and a minimum 4.41ºC at 2022-07-16 04:00:00. The same station data defines three heat wave periods during the survey, Heatwave from, 2022-07-08 to 2022-07-20, 2022-07-24 to 2022-07-27 and 2022-07-31 to 2022-08-03. Incoming shortwave radiation, humidity and wind speed varied substantially over the survey period, providing the primary drivers of near-surface temperature dynamics analysed in subsequent section.

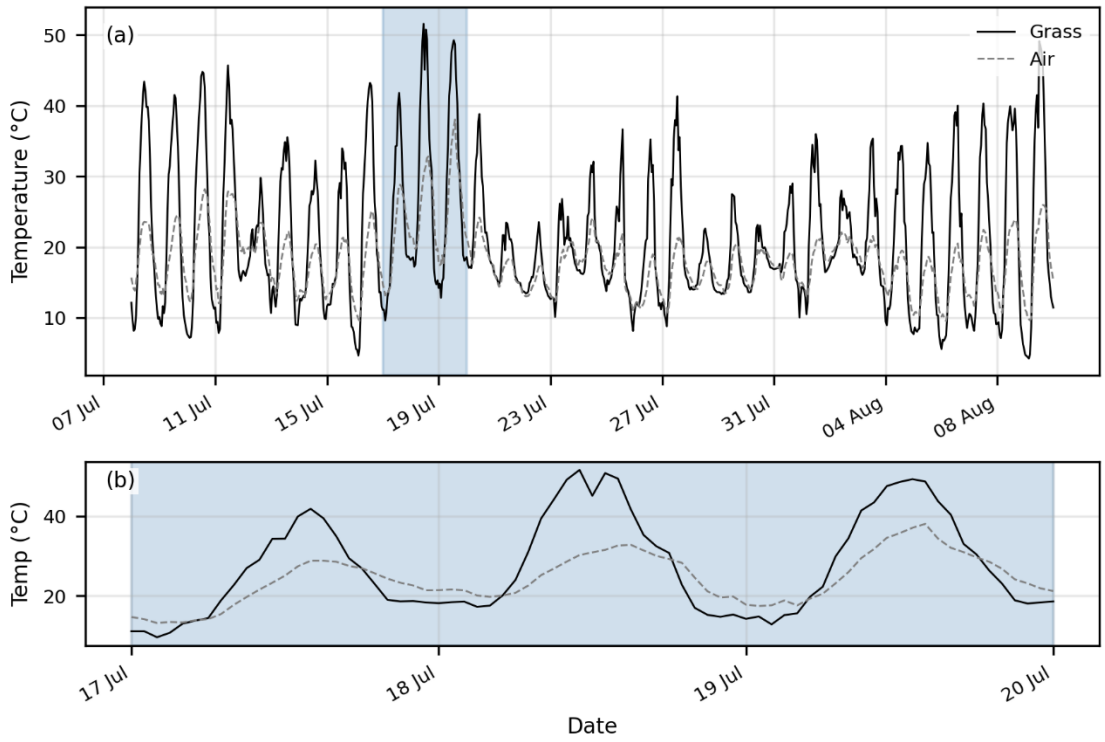

Figure 4. Time series of grass (solid black line) and air (dashed line) temperatures measured at RAF Leeming during the study period. (a) Full record from 7 July to 10 August 2022 showing strong diurnal variability in both grass and air temperatures. The light blue shading highlights the period of 17–20 July, which is expanded in (b). (b) Four-day zoom-in (17–20 July 2022) illustrating diurnal temperature cycles during the July 2022 heatwave, with daytime grass temperatures frequently exceeding 40 °C and substantially exceeding air temperatures.

3.2 Temperature Bias Correction

The raw temperature measurements exhibited a positive relationship with Mean DC offset across three nodes used for bias correction. The Mean DC increased systematically with increasing temperature, whereas RMS amplitude showed only weak associations with temperature. The relationship between Mean DC and temperature was consistent across the three nodes examined. Correlations between temperature and operational metrics were generally weak ($r < 0.21$ for RMS amplitude, timing corrections, synchronization corrections and data-gap statistics), while a moderate positive correlation was observed between temperature and Mean DC offset ($r = 0.61$) (see Supplementary Material 2)

Several machine-learning models were evaluated to correct the systematic bias between microcontroller die temperature and ambient environmental temperature, including Random Forest, Extra Trees, and gradient boosting approaches. The gradient boosting models performed best, with the subsampled GBT achieving the highest accuracy, followed by the histogram-based variant (Table 1). Tree-based ensemble methods (Random Forest and Extra Trees) showed lower performance and higher error (Table 1). Differences in bias structure and diurnal behaviour remained evident. Boosting

approaches produced near-zero mean bias (−0.004 to −0.067°C), whereas Random Forest and Extra Trees exhibited systematic positive bias (~+1.26 to +1.34°C). These differences were most pronounced in the diurnal cycle: boosting approaches captured stronger nocturnal cooling and more moderate daytime heating, while bagging-based models overestimated daytime heating and underestimated nocturnal cooling (Table 1). Additionally, Random Forest and Extra Trees produced higher maximum temperatures, indicating likely overestimation of extremes relative to boosting approaches. Although performance differences between GBT and HGBT models were modest, the GBT model was selected for subsequent analysis due to its slightly improved predictive performance and consistent behaviour. All corrected temperatures presented subsequently use the subsampled GBT model.

Model	R2	MSE	Bias mean	Bias std	Day mean	Night mean	Max temp	Diurnal range	Bias mean
GBT	0.922	3.143	-0.004	6.509	2.795	-6.045	63.048	8.84	0.004
HGBT	0.912	3.578	-0.067	6.495	2.738	-6.122	62.818	8.86	0.067
RF	0.882	4.78	1.342	6.297	3.988	-4.371	63.95	8.359	1.342
ET	0.882	4.807	1.258	6.357	3.898	-4.439	64.13	8.336	1.258

Table 1. Comparison between regression model performance. GBT: Gradient boosted tree with subsampling; HGBT: Histogram boosted tree; RF: Random Forest; ET: Extra trees

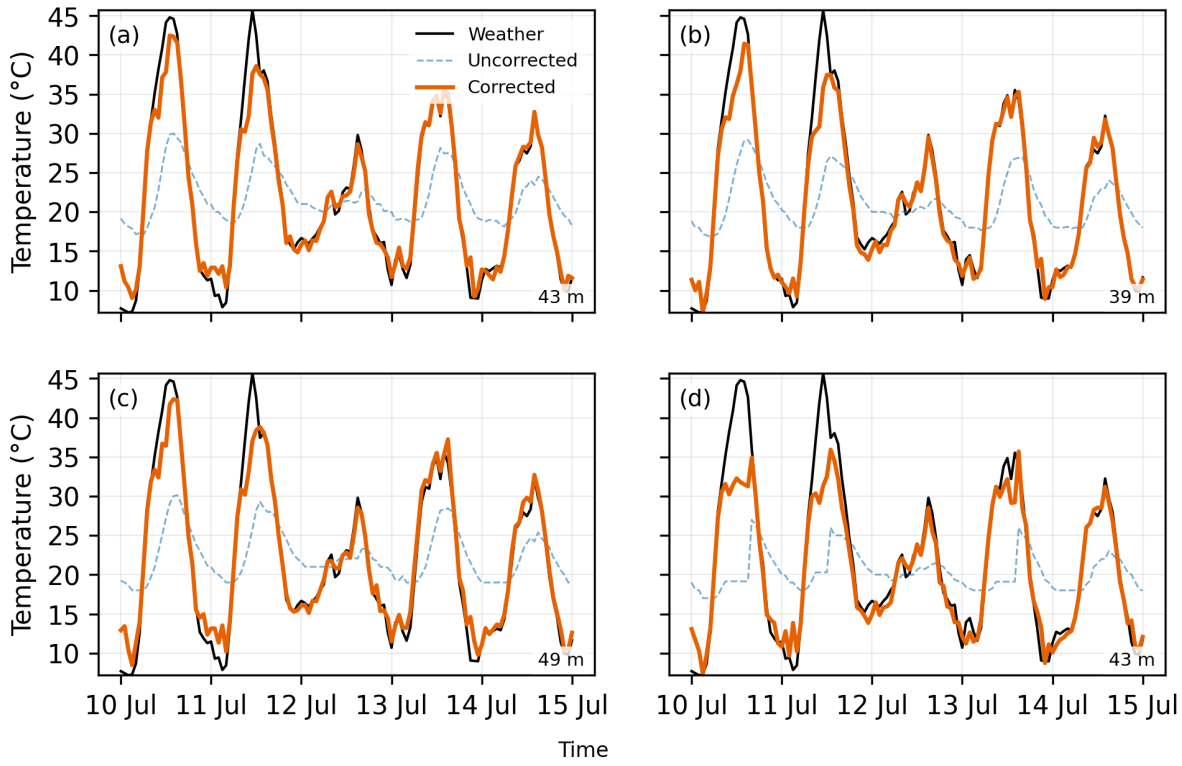

Figure 5. Comparison of uncorrected and corrected microcontroller die temperatures with reference grass temperature measurements from the meteorological station. (a-c) three sensors, 2300042571, 2300037527, 2300041806 respectively, used to train the GBT correction model. (d) nearest sensor, 2300113496, excluded from model calibration. The correction substantially reduces the daytime warm bias and improves agreement with the reference temperature record.

3.3 Temporal Characteristics of Near Surface Temperatures

3.3.1 Diurnal Behaviour and Extremes

The three sensors used for training the models were located within 50 m of the reference meteorological station and the corrected temperatures more closely reproduce the magnitude and temporal variability of the reference grass temperature than the uncorrected microcontroller die temperatures (Figure 5 a-c). Similar behaviour is observed for both the calibration sensors (Figure 5a-c) and the nearest sensor (serial 2300033336) not used during model training (Figure 5d). The corrected temperature at this sensor exhibits comparable extremes relative to the meteorological observations, with a maximum of 44.9 °C and a minimum of 6.7 °C.

Across the full sensor network, the maximum corrected temperature was 63.1 °C (serial 2300057433), while the minimum was −3.1 °C (serial 2300030249). The maximum diurnal temperature range was 26.8 °C (serial 2300035843), indicating substantial

temporal variability in near-surface conditions, whereas the minimum diurnal range was 12.3 °C (serial 2300041694).

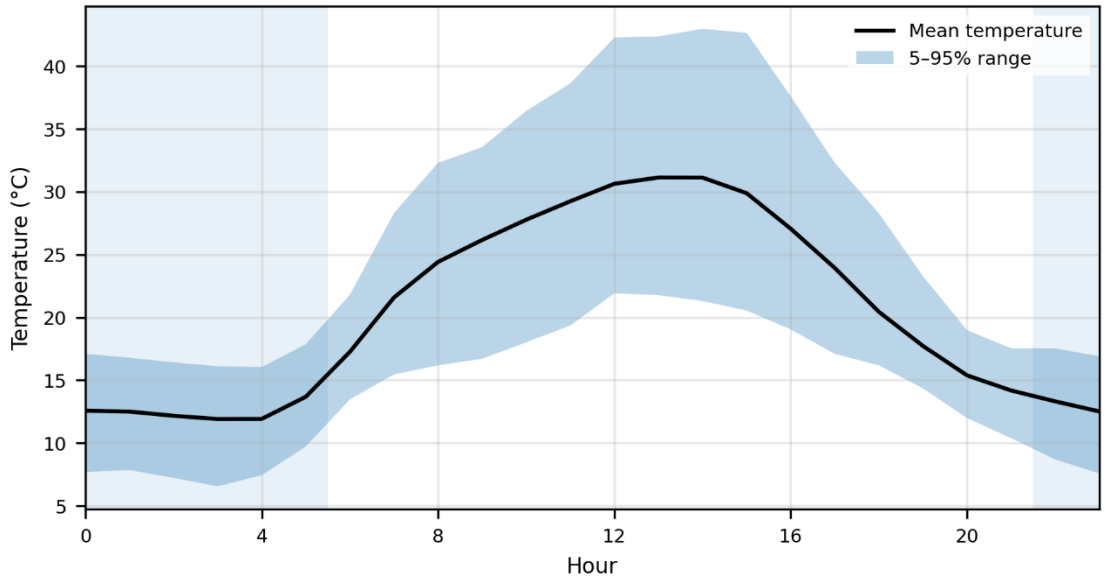

Figure 6. Diurnal Behaviour and Extremes, the light blue shading represents the 'nighttime' hours.

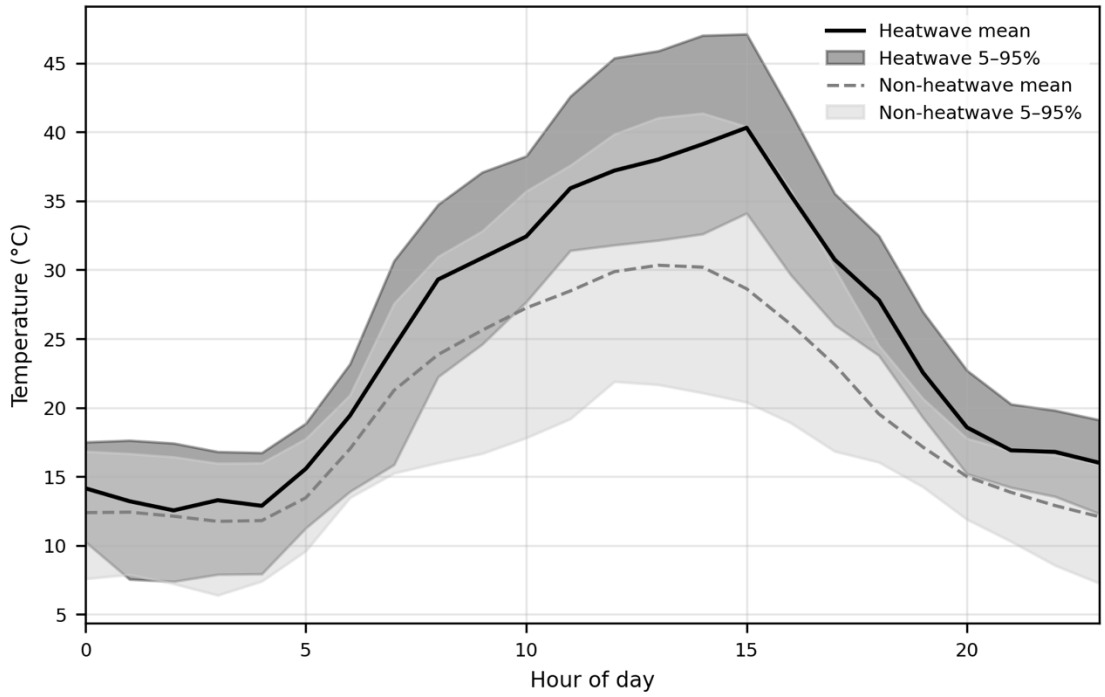

Figure 7. Diurnal behaviour split by heatwave days and non-heatwave days.

3.3.2 Spatial contrasts during extreme conditions

Spatial temperature variability, quantified using pairwise temperature differences (ΔT), shows clear contrasts across regimes and spatial scales. At the adjacent scale (≤15 m), mean ΔT is highest during heatwave daytime conditions (1.89°C), compared to non-heatwave daytime (1.28°C), indicating enhanced fine-scale thermal heterogeneity during

extreme heating. This contrast is less pronounced at night, where heatwave conditions exhibit lower variability (1.41°C) than non-heatwave conditions (1.52°C). At the larger (range) scale (80–200 m), mean ΔT increases across all regimes, with heatwave daytime again showing the strongest spatial gradients (2.36°C), followed by non-heatwave daytime (1.49°C). Night-time variability remains lower overall, with heatwave night (1.66°C) and non-heatwave night (1.70°C) showing similar magnitudes.

The distributions of pairwise temperature differences also vary between regimes. During heatwave daytime conditions, the upper tail of the distribution is substantially elevated, with p95 values reaching 3.67°C (adjacent) and 4.80°C (range), compared to 2.99°C and 3.72°C respectively under non-heatwave conditions. Maximum observed ΔT values are also elevated during daytime, particularly at the range scale (5.48°C for heatwave vs 5.36°C for non-heatwave), indicating the occurrence of strong localised thermal contrasts. In contrast, night-time distributions are more constrained, with lower p95 values (≤2.36°C) and reduced maxima, especially during heatwave conditions where variability is notably suppressed (maximum 1.94°C at adjacent scale). Overall, these results indicate that heatwave conditions amplify spatial thermal heterogeneity during the day, while promoting more spatially uniform conditions at night.

Regime	Scale	Mean	Median	p95	max
Heatwave day	adjacent	1.89	1.66	3.67	4.19
Heatwave day	range	2.36	2.00	4.80	5.48
Heatwave night	adjacent	1.41	1.32	1.89	1.94
Heatwave night	range	1.66	1.55	2.26	2.31
Non heatwave day	adjacent	1.28	1.05	2.99	4.36
Non heatwave day	range	1.49	1.20	3.72	5.36
Non heatwave night	adjacent	1.52	1.50	2.08	3.29
Non heatwave night	range	1.70	1.73	2.36	4.97

Table 2. Statistical comparison of corrected temperatures at different distances and times. Adjacent refers to between pairs 10m apart, range refers to pairs between 100 and 300m apart.

3.3.3 Forcing response relationships

The gradient boosting model demonstrated strong predictive performance on withheld observations (R^2 = 0.92, MAE = 1.38 °C, RMSE = 1.77 °C, MBE = -0.27 °C). These metrics should be interpreted in the context of the limited calibration dataset and the temporal autocorrelation inherent within environmental time series. In the uncorrected data, radiation exhibited a relatively strong positive correlation with temperature change (mean r = 0.346), while wind speed and humidity showed weak and variable relationships (mean r = 0.008 and r = 0.009, respectively), with approximately equal proportions of positive and negative values. Following correction, the correlation with radiation was substantially reduced (mean r = 0.020), while wind showed a consistent negative

correlation (mean r = -0.123, 0% positive) and humidity a consistent positive correlation (mean r = 0.229, 100% positive) across sensors. Correlations with meteorological variables were generally consistent across the sensor network, with temperature showing positive relationships with solar radiation and negative relationships with humidity (**Figure 8**). Temporal lag analysis indicated that these responses occurred with little delay, suggesting that corrected temperatures primarily reflect contemporaneous environmental conditions. Because radiation is included as a predictor in the correction model, relationships involving radiation are not fully independent. The observed reduction in temperature–radiation correlation therefore reflects, in part, the model's removal of radiation-related bias and is consistent with the removal of radiation related artefacts.

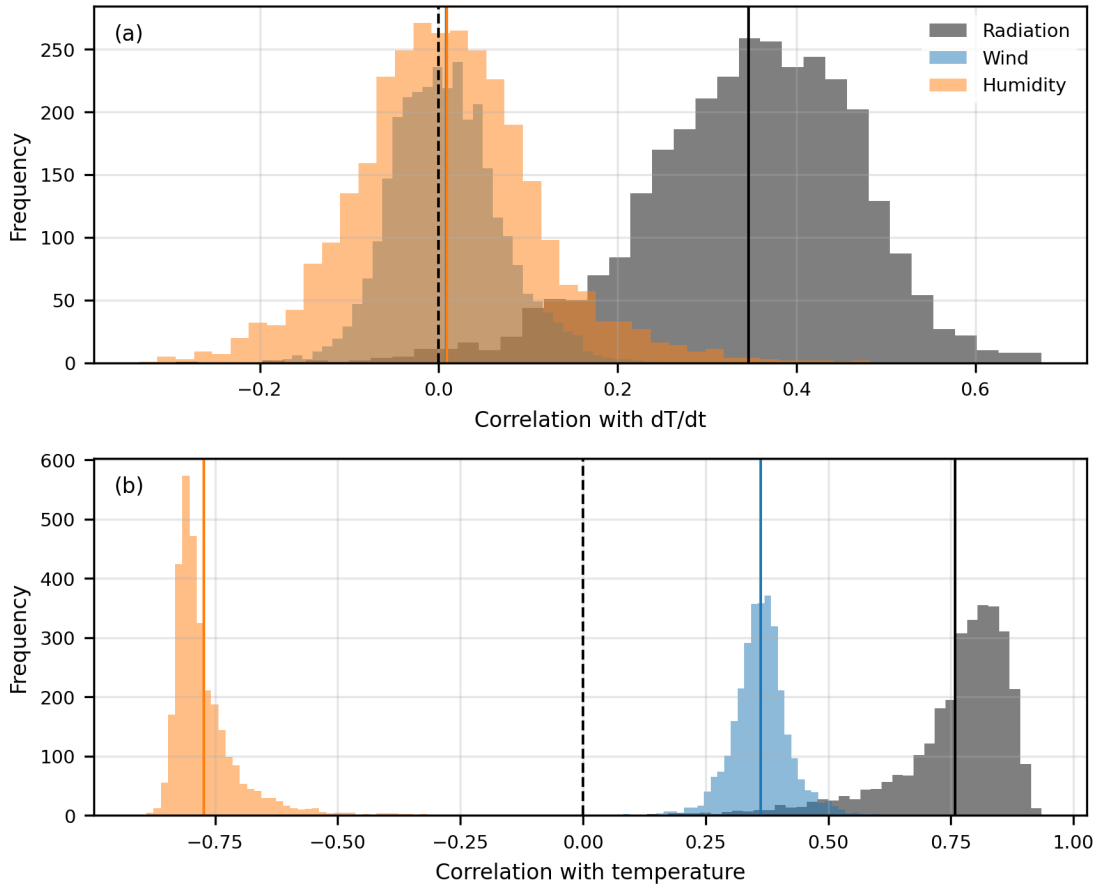

Figure 8. Distribution of correlations between temperature change (dT/dt) and radiation, wind and humidity as measured at the weather station.

3.4 Spatial Variability in Temperature Response

Spatial structure exhibits clear regime dependence, as indicated by both variogram metrics (**Figure 9**) and Moran's I. Variogram analysis shows that correlation lengths are short during daytime conditions, with median ranges of approximately 90 m for both heatwave and non-heatwave periods. Although substantial temporal variability is present (95% interval 70–415 m during heatwaves and 10–370 m during non-heatwave periods), the typical spatial correlation scale remains short. Correlation lengths increase substantially at night, reaching median values of ~170 m under non-heatwave conditions (95% interval 50–452 m) and ~270 m during heatwaves (95% interval 90–520 m), indicating greater spatial coherence of nighttime temperature fields. In contrast, sill values are highest during heatwave daytime conditions (median ~4.8 °C^2; mean ~6.7 °C^2), indicating strong spatial variability, and lowest during non-heatwave daytime conditions (median ~1.3 °C^2). These patterns are consistent with Moran's I, which indicates generally weak but non-zero spatial autocorrelation across all regimes, with slightly higher values at night and during heatwave conditions, demonstrating that the temperature fields are characterised by short-range spatial dependence with a substantial local variance component.

Local Moran's I (LISA) analysis further demonstrates that this spatial structure is highly heterogeneous and spatially fragmented. Approximately 26% of sensors exhibit statistically significant local autocorrelation ($p < 0.05$), with High–High and Low–Low clusters accounting for ~20% of observations, indicating the presence of localised zones of coherent warming and cooling. However, the majority of sensors (~74%) show no significant spatial association, confirming that spatial dependence is limited in extent. The presence of High–Low and Low–High outliers (~7%) further indicates sharp local gradients, consistent with fine-scale variability in surface and microclimatic conditions.

The spatial variability from variogram analysis and LISA results show that while temperature fields exhibit identifiable spatial organisation, this structure is patchy and confined to relatively short distances. To assess whether the correction procedure altered the underlying spatial organisation of temperatures, LISA analyses were performed on both corrected and uncorrected datasets. Cluster classifications showed high agreement between datasets (mean agreement 85–96% across all regimes), indicating that the correction primarily adjusted temperature magnitudes while preserving the dominant spatial patterns. This suggests that the observed thermal

patchiness and clustering are inherent features of the temperature field rather than artefacts introduced by the bias-correction procedure.

Spatial coherence increases under nocturnal and heatwave conditions, but remains insufficient to produce a fully continuous spatial field, with local heterogeneity dominating the observed temperature patterns.

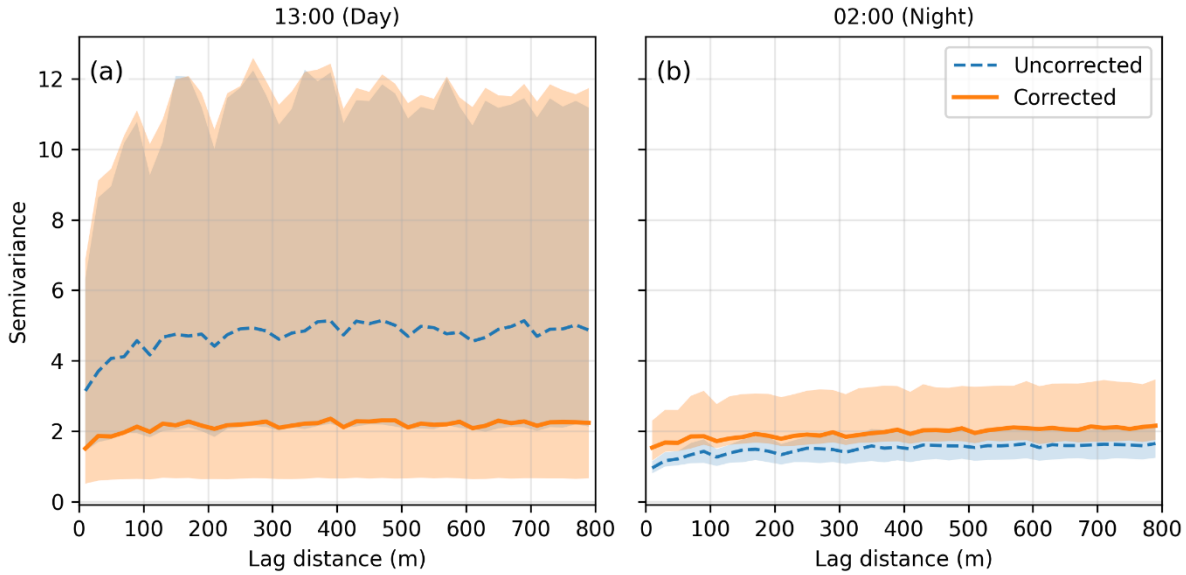

Figure 9. Variograms for day and night showing both uncorrected and corrected temperature data.

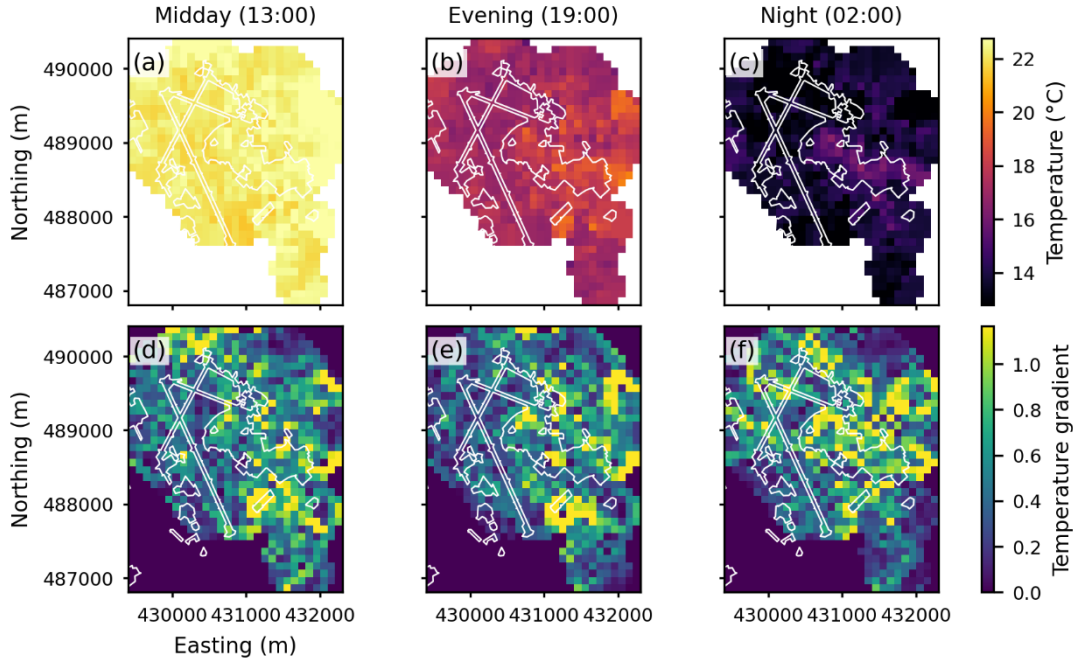

Figure 10. Representative gridded maps of temperature across the survey area. White polygon represents the aggregated outline of the built-up urban areas across the survey area.

Near-surface temperature fields exhibit pronounced fine-scale heterogeneity. Correlation lengths are short during daytime conditions (~90 m median range), indicating that thermal anomalies are spatially confined and highly localised. At night, correlation lengths increase substantially (~170–270 m), reflecting a transition towards more spatially coherent temperature fields. Spatial variability remains substantial ($\sigma \approx 2.2$ °C; equivalent to typical cross-site differences of several degrees). Spatial autocorrelation is generally weak at the sensor scale due to strong local variability, but coherent clustering emerges when observations are aggregated over distances exceeding ~50 m. Together, these results demonstrate a clear day–night transition from patchy local thermal structure to broader, more organised spatial patterns. Gridded temperature show clear day – night differences, transitioning from patchy local structure to broader more organised patterns (**Figure 10**).

Multi-scale LISA analysis demonstrates strong scale dependence in spatial clustering (**Figure 11** and **Figure 12**). The proportion of sensors exhibiting statistically significant local spatial association increases systematically with neighbourhood size across all regimes, indicating that fine-scale thermal heterogeneity is embedded within broader coherent structures. Heatwave night conditions exhibit the strongest spatial organisation, with significant clustering increasing from 0.26 at k = 4 to >0.9 at k = 1024. In contrast, daytime regimes remain comparatively heterogeneous, with lower clustering fractions across equivalent scales. Significant associations are dominated by High–High and Low–Low clusters, whereas High–Low and Low–High outliers remain relatively uncommon, indicating persistent hotspot and cool-zone structures across multiple spatial scales.

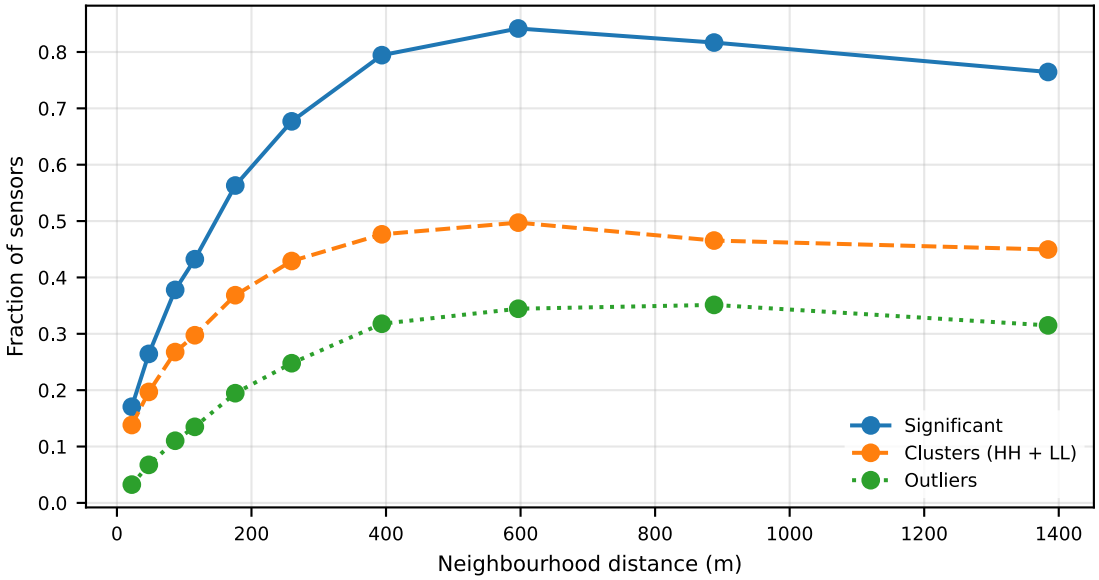

Figure 11. Fraction of sensors exhibiting significant spatial association, coherent clusters (High – High and Low - Low), and spatial outliers (High – Low and Low -High) as a function of neighbourhood distance

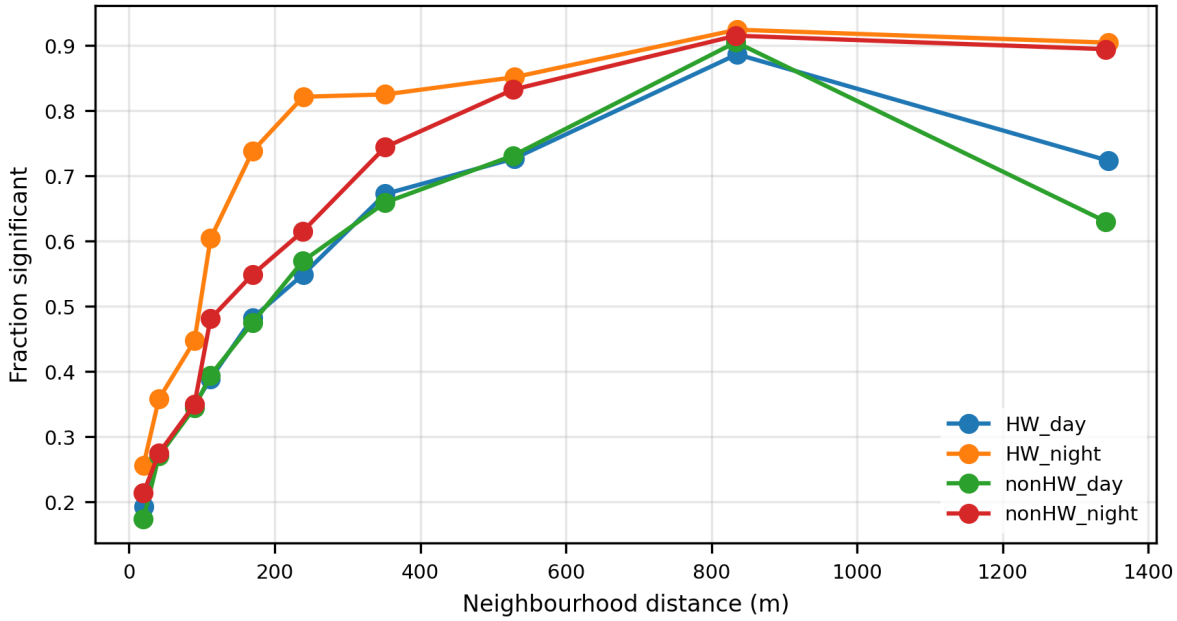

Figure 12. Fraction of sensors classified as statistically significant local clusters (High–High and Low–Low) and spatial outliers (High–Low and Low–High) as a function of neighbourhood size for heatwave (HW) and non-heatwave (nonHW) daytime and nighttime temperature fields.

regime	N_sensors	N_timesteps	cluster50_distance_m	HH_at_50pct	LL_at_50pct
HW_day	3072	55	239.2	0.147	0.197
HW_night	3072	55	112.0	0.231	0.211
nonHW_day	3083	360	238.8	0.139	0.226
nonHW_night	3083	360	169.5	0.192	0.182

Table 3. Summary table of LISA statistics for aggregated mean temperatures. N_sensors = number of sensors; N_timesteps = number of observations used to calculate the mean field; cluster50_distance_m = neighbourhood distance at which significant local clustering exceeds 50% of sensors; HH_at_50pct and LL_at_50pct = fractions of sensors belonging to High–High and Low–Low clusters, respectively, at that scale.

3.5 Influence of Environment and Land Use on Thermal Variability

The distribution of temperature anomalies varies systematically across land-use classes, as shown in **Figure 13** and summarised in **Table 4**. Thermal anomalies exhibit strong land-use and diurnal dependence. Built-up areas show a pronounced reversal between daytime and nighttime conditions, with negative mean anomalies during the day (≈ −0.35 °C) but positive anomalies at night (≈ +0.29 °C) relative to the woodland reference class. In contrast, improved grassland exhibits consistently negative anomalies during both daytime and nighttime periods, with the strongest cooling observed nocturnally (≈ −0.32 °C). Persistence metrics similarly demonstrate enhanced nocturnal thermal retention

within built environments, where positive anomalies occur more frequently (≈0.61) than in grassland environments (≈0.34). Differences are also evident in the upper tails of the distributions, with built-up areas exhibiting elevated nighttime extremes (p95 ≈ 1.90 °C), whereas grassland environments display comparatively suppressed nocturnal extremes (p95 ≈ 0.82 °C). Woodland environments exhibit the greatest overall variability (σ ≈ 1.09–1.11 °C), reflecting strong local thermal fluctuations around the reference condition. Together, these results indicate that land-use controls on temperature anomalies are strongly regime dependent and are dominated by nocturnal heat retention and persistence rather than daytime mean temperature contrasts alone. The persistence metrics are unlikely to be substantially influenced by thermal inertia of the sensor housing. As an example, for one of the sensors used in the GBT model, the mean absolute temperature-change rates recorded by the node and the reference weather station were 2.19 °C h^{-1} and 2.15 °C h^{-1}, respectively, yielding a ratio of 1.02. Hourly temperature-change rates were also strongly correlated (r = 0.79), indicating similar rates of warming and cooling between the node and the reference station.

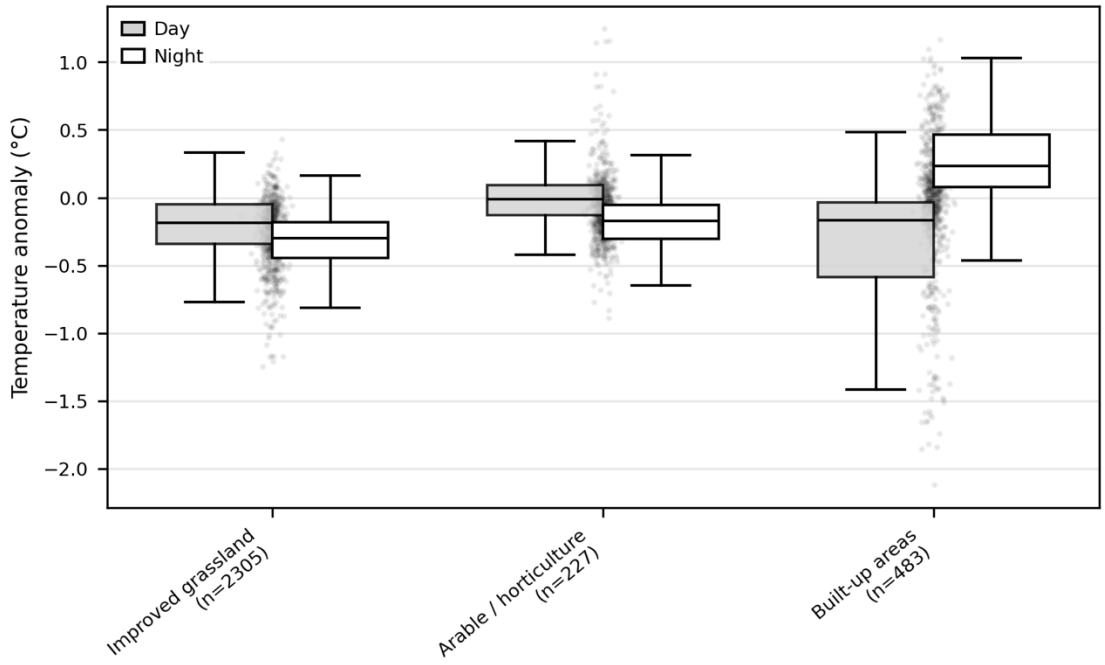

Figure 13. Box plot of mean daily temperature anomaly by land use classification

Land use type	period	mean	ci95_low	ci95_high	std	persistence	p95	N_values	n_sensors
Arable / horticulture	day	0.022	-0.004	0.049	0.251	0.446	0.498	344	227
Arable / horticulture	night	-0.181	-0.201	-0.161	0.192	0.405	0.118	343	227
Broadleaf woodland	day	-	-	-	-	0.464	-	344	68
Broadleaf woodland	night	-	-	-	-	0.457	-	343	68
Built-up areas	day	-0.351	-0.402	-0.299	0.485	0.360	0.131	344	483
Built-up areas	night	0.287	0.258	0.317	0.281	0.605	0.791	343	483
Improved grassland	day	-0.239	-0.269	-0.209	0.285	0.357	0.122	344	2305
Improved grassland	night	-0.322	-0.343	-0.300	0.202	0.336	-0.034	343	2305

Table 4. Summary of temperature anomaly by land use type

4 Discussion

This study presents what is thought to be the highest density of in situ surface temperatures reported to date, comprising over 80 million measurements from 3,083 sensors covering 6 km^2. The dataset is unique in that it coincides with an extreme heatwave, capturing conditions rarely observed at such spatial resolution. This unique dataset enables quantification of the sub 100 m variability including spatial contrasts and capturing the diurnal evolution of heterogeneity. The data demonstrate the potential of using incidental environmental measurements from non-dedicated sensors to complement existing crowdsourced weather data and the associated corrections which often rely on machine-learning algorithms (e.g. Beele et al. 2022, Brousse et al. 2023).

Previous studies have shown that within cities air temperature differences can reach ~8–9 °C during extreme heat events, indicating substantial spatial variability at the urban scale (Cao et al., 2021). The results here demonstrate differences of several degrees also occur over distances of tens of metres, revealing significant thermal heterogeneity exists at much finer spatial scales than typically resolved. This suggests that urban temperature variability is not only a large-scale phenomenon but is also strongly expressed at sub 100 m scales. The fine-scale variability identified here highlights the potential for remotely sensed land surface temperature (LST) products to overlook local temperature contrasts because they represent spatially aggregated surface conditions.

4.1 Measurement artefacts and thermal response

The uncorrected sensor data exhibit strong correlations with radiation and weak or inconsistent relationships with wind speed and humidity, that are interpreted as indicating the temperatures respond primarily to radiative exposure and diurnal covariance. The absolute values are modified by the thermal characteristics of the seismic node housing. The housing modifies the radiative environment experienced by the temperature sensor and introduces some thermal buffering, resulting in a reduced diurnal temperature range relative to the reference weather station. Daytime maxima are likely moderated by shielding of the internal temperature sensor from direct solar radiation, while slightly elevated nocturnal temperatures may reflect reduced radiative cooling and a small background thermal offset associated with the node electronics and enclosure. Comparison of hourly temperature change rates between the nearest node not used in calibration (2300033336) and the reference weather station showed very similar rates of warming and cooling (2.19 and 2.15 °C h^{-1}, respectively), indicating that the sensor housing is unlikely to introduce substantial delays in thermal response. Radiation-induced bias in unshielded sensors is strongly correlated with diurnal temperature range (Berk et al., 2025; Yang et al., 2025). The raw sensor temperature reflects both environmental forcing and biases associated with radiative exposure and

602 the thermal properties of the housing. The GBT correction accounts for systematic
603 measurement biases associated with radiative exposure and sensor configuration,
604 improving the correspondence between node temperatures and external environmental
605 forcing.

606

607 **4.2 Limitations of analysis**

608 The results demonstrate consistent differences in surface temperatures across land-use
609 classes, particularly in terms of persistence and extremes. However, there are limitations
610 in calibration and data resolution that constrain the extent to which these dynamics can
611 be fully resolved from this survey data.

612 While sub-hourly sensor data reveal rapid thermal dynamics, attempts to apply
613 correction models at this resolution are limited by the temporal resolution of the
614 calibration data. In this study, only the temperatures from meteorological station were
615 available on sub hourly intervals, with all other properties, including radiation, available
616 only at hourly intervals. Consequently, efforts to apply sub-hourly correction did not yield
617 as reliable estimates of temperature change rates. However, the raw sensor data indicate
618 the presence of high-frequency variability, indicating that, with appropriately resolved
619 meteorological forcing (e.g. sub-hourly radiation and atmospheric measurements),
620 dense sensor networks could be calibrated to capture fine-scale temporal dynamics.

621 While the temperature reflects the thermal state of the device rather than ambient air
622 temperature directly there is limited evidence to indicate that internal electronic heating
623 influences the recorded temperatures (see Supplementary Material 2). The positive
624 relationship observed between internal temperature and Mean DC offset is interpreted
625 as temperature-dependent drift in electronic offsets within the acquisition circuitry
626 rather than evidence of temperature changes induced by node activity. Although Mean
627 DC offset increased with temperature, it is a diagnostic metric and not a direct indicator
628 of energy consumption. The weak association between temperature and RMS signal
629 amplitude suggests that the node activity did not systematically coincide with higher
630 temperatures. We conclude that environmental forcing, rather than operational self-
631 heating, dominates the recorded temperature signal.

632 The correction model was developed using 1,914 hourly observations (1,530 used for
633 training) from three calibration sensors. While this provides sufficient data for tree-based
634 learning, the effective sample size is reduced by temporal autocorrelation. A limitation of
635 the approach is that calibration data were derived from sensors located within a relatively
636 small area surrounding a single reference station. Consequently, the model assumes
637 that the relationship between microcontroller die temperature and ambient
638 environmental temperature remains consistent across the wider survey area and under
639 different local environmental conditions. While the calibration produced internally

consistent results across the array, future deployments should evaluate calibration performance across a broader range of land-use types and microclimatic settings to determine whether a single reference station is sufficient or whether multiple calibration locations are required to account for spatially variable environmental influences on sensor behaviour.

More broadly, calibration is derived from a limited subset of locations and is not explicitly stratified across land-use types, meaning that potential land-use-specific biases in sensor response or microclimatic forcing may not be fully resolved. This is particularly relevant for unshielded low-cost temperature sensors, which can exhibit non-linear biases associated with solar radiation loading, housing thermal inertia, and diurnal temperature range. Berk et al., (2025) demonstrated that such biases can vary systematically with environmental conditions and may not be fully removed through calibration against a single reference station. Consequently, while the broad spatial patterns, land-use differences, and clustering behaviour identified in this study are considered robust, the magnitude of the most extreme daytime temperature anomalies and upper-tail statistics should be interpreted with appropriate caution.

In addition, land-use classification was based on broad polygon datasets that may not capture fine-scale heterogeneity at the resolution of the sensor deployment (e.g. 10m), and corrected temperatures were not independently validated against additional in situ reference measurements. These limitations indicate that the results should be interpreted as a demonstration of capability rather than a definitive quantification of land-use effects.

With appropriate calibration, temperature measurements from embedded microcontroller sensors could provide a low-cost, scalable complement to conventional meteorological monitoring networks. Future work should consider implementing a metadata-based quality control protocol, as seen in dense crowdsourced weather networks such as 'Leuven.cool' (Beele et al., 2022) or Netatmo-based studies (Chapman et al., 2016). This could further improve distinguishing environmental signal from artifacts based on siting characteristics (e.g., proximity to buildings, sensor height).

4.3 Magnitude and structure of spatial temperature variability

The results demonstrate strong regime dependence in both the magnitude and spatial organisation of near-surface temperature variability, consistent with behaviour reported in existing studies of urban climate systems (e.g. Roth et al., 2022). Spatial temperature differences are largest during daytime heatwave conditions and substantially reduced at night, consistent with behaviour reported in urban climate studies and numerical modelling experiments (Shreevastava et al., 2021). During daytime heatwave conditions, mean temperature differences reach approximately 3.0 °C at broader spatial scales and

2.35 °C between adjacent sensors, compared with approximately 2.3 °C and 1.91 °C respectively during nighttime periods. Extreme contrasts are also observed, with maximum differences exceeding 17 °C during peak daytime heatwave conditions. Upper-end temperature differences (95th percentile) remain high during daytime heatwaves, reaching approximately 7.7 °C at broader spatial scales and 5.9 °C at adjacent scales, indicating that substantial thermal contrasts occur across large portions of the study area rather than being restricted to isolated outliers.

Spatial analyses further demonstrate that the temperature field is structured rather than random. Variogram analysis indicates short daytime correlation lengths (~90 m median range) and substantially longer nighttime correlation lengths (~170–270 m), reflecting a transition from locally heterogeneous daytime conditions to more spatially coherent nighttime temperature fields. Multi-scale LISA analysis similarly shows that coherent thermal clustering strengthens systematically with neighbourhood scale, with nighttime heatwave conditions exhibiting the strongest spatial organisation. More than 90% of sensors exhibit statistically significant local clustering at the largest neighbourhood scales during nighttime conditions, while daytime conditions remain comparatively fragmented and locally variable. Cluster analysis also identifies persistent high-high and low-low thermal regions, indicating that coherent hotspots and cool zones emerge across the landscape rather than forming purely stochastic spatial patterns.

The observed land-use dependence provides a likely mechanism for these spatial behaviours. Built-up areas exhibit a strong diurnal reversal, with negative daytime anomalies relative to woodland environments but positive nighttime anomalies and substantially greater nocturnal persistence. In contrast, grassland environments exhibit consistently negative anomalies and reduced nighttime persistence, indicating more efficient cooling and reduced thermal storage. These contrasts suggest that the observed nighttime spatial coherence is partly driven by differential thermal retention between land-use classes, producing organised mesoscale thermal structures that persist after sunset. During daytime heatwave conditions, however, strong radiative forcing and fine-scale surface heterogeneity generate highly localised temperature contrasts that reduce overall spatial coherence despite large thermal gradients.

The dense sensor array captured fine-scale thermal heterogeneity that may not be resolved by conventional remote sensing approaches or coarser monitoring networks. Although remotely sensed land surface temperature products commonly identify broad urban-rural thermal gradients, the present results demonstrate that substantial temperature variability persists at scales below ~100 m, particularly during daytime heatwave conditions. Consequently, assessments of heat exposure, ecosystem stress, and thermal refugia based solely on coarse spatial products may underestimate the magnitude and persistence of local thermal contrasts experienced at scales relevant to ecosystems and human exposure.

4.4 Implications for modelling approaches

Many models of urban climate and meteorological conditions for human health or ecology are developed to produce results at km-scale resolution, with models used for human health extending to down to ~250 m resolution (Schinasi et al., 2018; e.g. Yi et al., 2022) and in ecology even down to 25 m (Kemppinen et al., 2024; Haesen et al., 2023). However rarely do comparative observational datasets with such high spatial resolutions exist. The equipment deployment here enabled distinguishing spatial heterogeneity as fine as 10 m between individual pairs and the reliable construction of gridded temperature maps with 100 m cell size. These data enable the identification of clear sub-kilometre variability and at hourly intervals. The results indicate that the use of incidental environmental sensing could provide a basis calibrating or independently validating modelling results.

The results also provide insights into the interaction between meteorological forcing and surface characteristics (Dickinson, 1995; Nicholson, 1988). Observations indicate diurnal and heatwave forcing dominate variability demonstrated by strong day–night contrast (~40% reduction at night) with the amplification of this during heatwave periods (~15–20%). The different land use types and surface characteristics act as secondary modifiers tending to influence magnitude, not primary structure. Spatial patterns reflect local response to atmospheric forcing, not static land classification alone. This implies that when aggregated land surface classification is useful first-order predictor of thermal behaviour, but is insufficient to explain short-term dynamics

The data here reveal short-lived but intense local temperature extremes that are unlikely to be captured by high temporal resolution from single meteorological station data, or from spatially extensive, but lower and temporal resolution averages from remote sensing. This has implications for understanding, for example, the public health risks associated with heat exposure (Pan et al., 2024), urban planning (Iungman et al., 2023) and ecosystem responses (Piano et al., 2017). The results from our study evidence that there are isolated and short-term local variability during heat wave events that current approaches may not capture.

4.5 Value of opportunistic and distributed sensing

The results demonstrate the feasibility of repurposing non-dedicated sensors for environmental monitoring, with obvious key advantages in terms of sensor density, spatial coverage, and cost-effectiveness. This suggests that existing distributed sensor networks represent a largely underutilised resource for characterising environmental conditions at high spatial resolution. These could also be utilized to verify existing

methods for correcting dense crowd-sourced weather data, such as spatially explicit ML-based corrections (Beele et al., 2022; Brousse et al., 2023)).

Calibration of low-cost environmental sensors using statistical and machine learning approaches is well established, with studies demonstrating substantial improvements in data quality through co-location with reference instruments and the inclusion of environmental predictors such as radiation and temperature (Nan et al., 2025). Recent work has also highlighted the importance of temporal correction and spatial consistency in distributed temperature measurements (Xu et al., 2025), reinforcing the need to address systematic sensor biases. There are limitations of unshielded, non-aspirated sensors, such as used in this study; specifically, the challenges regarding thermal inertia and residual radiation bias that persist despite statistical correction, and as recent work (e.g. Yang et al., 2025) suggests these can impact measurements even after correction.

There is significant potential to integrate the use of non-dedicated sensing with existing IoT networks and infrastructure monitoring systems, to enable dense, cost-effective environmental sensing at spatial scales that are difficult to achieve using conventional meteorological instrumentation alone. This study demonstrates that temperature measurements acquired by semiconductor temperature sensors embedded within geophysical instrumentation can provide meaningful environmental observations alongside their primary function. For geophysical surveys, opportunities exist to exploit temporary high-density terrestrial arrays, such as in seismic acquisition, for microclimate and meteorological monitoring, while similar approaches could potentially be extended to the marine environment, where ocean-bottom seismic instrumentation may provide complementary observations of seafloor temperature variability. More broadly, the widespread deployment of instrumented sensor networks for engineering, and infrastructure monitoring suggests an opportunity to develop large-scale opportunistic environmental observing systems that leverage existing hardware and deployments rather than relying solely on dedicated meteorological networks.

5 Conclusions

This study demonstrates the feasibility of using dense networks of non-dedicated sensors to resolve surface temperature variability at spatial and temporal scales that are not routinely captured by conventional meteorological instrumentation or satellite observations. By repurposing temperature measurements from microcontrollers within over 3,000 nodal seismometers, and applying a statistical bias-correction, it has been possible to characterise micro-scale thermal variability across a 6 km^2 area during an extreme heat event.

The analysis shows that raw sensor measurements are strongly influenced by radiative exposure effects, resulting in inflated relationships with radiation and weak or

inconsistent responses to other meteorological variables. Application of a machine learning–based correction substantially reduces radiative and exposure-related artefacts and yields a temperature signal that is consistent with co-located weather observations. Although differences in sensor configuration and enclosure design result in a reduced diurnal temperature range relative to the reference station, comparison of warming and cooling rates indicates that the sensor nodes respond rapidly to environmental temperature variations. Nevertheless, some uncertainty remains regarding the influence of sensor exposure and enclosure characteristics on the absolute magnitude of temperature extremes.

The work highlights the potential of leveraging existing distributed sensor networks as a cost-effective approach to environmental monitoring, offering significant advantages in terms of spatial density and coverage. Application of a Gradient Boosting Tree correction substantially reduced radiation-related measurement artefacts and produced temperatures that closely matched reference observations. The corrected dataset revealed strong fine-scale thermal heterogeneity, with temperature differences exceeding 5 °C over distances of only a few hundred metres during heatwave conditions and substantially greater nocturnal thermal persistence within built-up areas than grassland environments (0.61 versus 0.34).

Such approaches complement conventional high-precision meteorological observations and provide new insight into thermal environments at scales relevant to human exposure, ecosystems and infrastructure. Future work should focus on improving calibration across a wider range of environmental conditions and land-use types, as well as integrating higher-temporal-resolution meteorological forcing to better resolve rapid thermal dynamics. More broadly, there is significant potential to extend this approach through integration with IoT and infrastructure monitoring systems, enabling large-scale, high-resolution environmental sensing using existing sensor deployments.

6 Acknowledgements

We thank the Royal Air Force and Ministry of Defence for their support and access to RAF Leeming, and their personnel who supported the geophysical deployment. We thank the Newcastle University students employed on campus (SEOC) who supported the deployment and retrieval of the geophysical survey. We thank STRYDE for providing support and expertise for the use of their seismic nodes, including during survey planning and acquisition and the specifics of the device performance.

7 Data availability

The data used in this study and ML models are available from the follow repositories:

- Hourly weather station observations [10.25405/data.ncl.32786229]
- Raw temperature records [10.25405/data.ncl.32785947]
- Corrected hourly temperatures [10.25405/data.ncl.32785986]
- Device operation metadata and Supplementary Material S2 [https://doi.org/10.25405/data.ncl.32786010]
- Land use classifications, building geometries, and the digital terrain model used in this study are available via Digimap [https://digimap.edina.ac.uk].
- Code used in the machine learning models and Supplementary Material S1 (parameters used in ML) [10.25405/data.ncl.32786229]

8 Author Contributions

Mark Ireland (MI): Conceptualization; Methodology; Software; Formal analysis; Writing – original draft; Writing – review & editing.

Hector Barnett (HB): Methodology; Software; Data curation; Writing – review & editing.

Abdullah Kahraman (AB): Writing – review & editing.

Charles Dunham (CD): Conceptualization; Methodology; Data curation; Writing – review & editing.

9 Funding

The field data acquisition, and initial data examination were undertaken as part of Project ViTAL, funded by the Defence Innovation Fund. The analyses presented here represent a secondary use of these data. Abdullah Kahraman is partly supported by the DARe Hub, funded by the UK Engineering and Physical Sciences Research Council (EPSRC) and the UK Department for Transport (Grant No. EP/Y024257/1).

10 Conflict of interest

The authors declare no competing interests.

11 References

Anon (n.d.) *What is a heatwave?* [Online] [online]. Available from: https://www.metoffice.gov.uk/weather/learn-about/weather/types-of-weather/temperature/heatwave (Accessed 13 April 2026).

Arachchige, K.G., Branch, P. & But, J. (2023) 'Evaluation of Correlation between Temperature of IoT Microcontroller Devices and Blockchain Energy Consumption in Wireless Sensor Networks', *Sensors*, 23(14), p. 6265.

Beele, E., Reyniers, M., Aerts, R. & Somers, B. (2022) 'Quality control and correction method for air temperature data from a citizen science weather station network in Leuven, Belgium', *Earth system science data*, 14(10), pp. 4681–4717.

Berk, S., Chakraborty, T. & Hsu, A. (2025) *Biases due to widespread use of low-cost sensors for urban heat stress assessments*,

Betts, A.K., Ball, J.H., Beljaars, A.C., Miller, M.J. & Viterbo, P.A. (1996) 'The land surface-atmosphere interaction: A review based on observational and global modeling perspectives', *Journal of Geophysical Research: Atmospheres*, 101(D3), pp. 7209–7225.

Brousse, O., Simpson, C., Kenway, O., Martilli, A., Krayenhoff, E.S., Zonato, A. & Heaviside, C. (2023) 'Spatially explicit correction of simulated urban air temperatures using crowdsourced data', *Journal of Applied Meteorology and Climatology*, 62(11), pp. 1539–1572.

Burke, I.C., Kaye, J.P., Bird, S.P., Hall, S.A., McCulley, R.L. & Sommerville, G.L. (2003) 'Evaluating and testing models of terrestrial biogeochemistry: the role of temperature in controlling decomposition', *Models in ecosystem science*, pp. 225–253.

Burton, C., Ciavarella, A., Kelley, D.I., Hartley, A.J., McCarthy, M., New, S., Betts, R.A. & Robertson, E. (2025) 'Very high fire danger in UK in 2022 at least 6 times more likely due to human-caused climate change', *Environmental Research Letters*, 20(4), p. 044003.

Cao, J., Zhou, W., Zheng, Z., Ren, T. & Wang, W. (2021) 'Within-city spatial and temporal heterogeneity of air temperature and its relationship with land surface temperature', *Landscape and Urban Planning*, 206p. 103979.

Chapman, L., Bell, C. & Bell, S. (2016) 'Can the crowdsourcing data paradigm take atmospheric science to a new level?: A case study of the Urban Heat Island of London quantified using Netatmo weather stations', *International Journal of Climatology*,

Davie, J.C.S., Falloon, P.D., Pain, D.L.A., Sharp, T.J., Housden, M., Warne, T.C., Loosley, T., Grant, E., Swan, J., Spincer, J.D.G., Crocker, T., Cottrell, A., Pope, E.C.D. & Griffiths, S. (2023) '2022 UK heatwave impacts on agrifood: implications for a climate-resilient food system', *Frontiers in Environmental Science*, 11.

Dickinson, R.E. (1995) 'Land-atmosphere interaction', *Reviews of geophysics*, 33(S2), pp. 917–922.

Earth Science Data Systems, N. (2025) *ECOSTRESS Land Surface Temperature and Emissivity Daily L2 Global 70m V001 | NASA Earthdata*.

Giorgi, F. & Avissar, R. (1997) 'Representation of heterogeneity effects in Earth system modeling: Experience from land surface modeling', *Reviews of Geophysics*, 35(4), pp. 413–437.

Haesen, S., Lenoir, J., Gril, E., De Frenne, P., Lembrechts, J.J., Kopecký, M., Macek, M., Man, M., Wild, J. & Van Meerbeek, K. (2023) 'Microclimate reveals the true thermal niche of forest plant species', *Ecology Letters*, 26(12), pp. 2043–2055.

Hawkins, E., Sutton, R. & Kendon, M. (n.d.) 'Communicating changes in the intensity of UK heatwaves', *Weather*, n/a(n/a), .

Howarth, C., Mcloughlin, N., Armstrong, A., Murtagh, E., Mehryar, S., Beswick, A., Ward, B., Ravishankar, S. & Stuart-Watt, A. (2024) *Turning up the heat: Learning from the summer 2022 heatwaves in England to inform UK policy on extreme heat*,

Huang, B., Wang, J., Song, H., Fu, D. & Wong, K. (2013) 'Generating high spatiotemporal resolution land surface temperature for urban heat island monitoring', *IEEE Geoscience and Remote Sensing Letters*, 10(5), pp. 1011–1015.

Hulley, G. & Hook, S. (2017) *MOD21A1N MODIS/Terra Land Surface Temperature/3-Band Emissivity Daily L3 Global 1km SIN Grid Night V006*.

Iungman, T., Cirach, M., Marando, F., Barboza, E.P., Khomenko, S., Masselot, P., Quijal-Zamorano, M., Mueller, N., Gasparrini, A. & Urquiza, J. (2023) 'Cooling cities through urban green infrastructure: a health impact assessment of European cities', *The Lancet*, 401(10376), pp. 577–589.

James, G., Witten, D., Hastie, T., Tibshirani, R. & Taylor, J. (2023) 'Tree-based methods', in *An introduction to statistical learning: with applications in python*. [Online]. Springer. pp. 331–366.

John, J. & Rein, G. (2025) 'Heatwaves and Firewaves: The Drivers of Urban Wildfires in London in the Summer of 2022', *Fire Technology*, 61(5), pp. 3451–3460.

Kay, G., Dunstone, N., Smith, D.M., Brown, S.J., Kent, C., Lockwood, J.F. & Scaife, A.A. (2025) 'Rapidly increasing chance of record UK summer temperatures', *Weather*, 80(8), pp. 268–276.

Kemppinen, J., Lembrechts, J.J., Van Meerbeek, K., Carnicer, J., Chardon, N.I., Kardol, P., Lenoir, J., Liu, D., Maclean, I., Pergl, J., Saccone, P., Senior, R.A., Shen, T., Słowińska, S., Vandvik, V., von Oppen, J., Aalto, J., Ayalew, B., Bates, O., et al. (2024) 'Microclimate, an important part of ecology and biogeography', *Global Ecology and Biogeography*, 33(6), p. e13834.

Kershaw, T., Sanderson, M., Coley, D. & Eames, M. (2010) 'Estimation of the urban heat island for UK climate change projections', *Building Services Engineering Research & Technology*, 31(3), pp. 251–263.

de La Flor, F.S. & Domınguez, S.A. (2004) ‘Modelling microclimate in urban environments and assessing its influence on the performance of surrounding buildings’, *Energy and buildings*, 36(5), pp. 403–413.

Maclean, I.M., Duffy, J.P., Haesen, S., Govaert, S., De Frenne, P., Vanneste, T., Lenoir, J., Lembrechts, J.J., Rhodes, M.W. & Van Meerbeek, K. (2021) ‘On the measurement of microclimate’, *Methods in Ecology and Evolution*, 12(8), pp. 1397–1410.

Met Office (2012) *Met office integrated data archive system (MIDAS) land and marine surface stations data (1853-current)*.

Met Office (n.d.) *What is a heatwave?* [Online] [online]. Available from: https://weather.metoffice.gov.uk/learn-about/weather/types-of-weather/temperature/heatwave (Accessed 23 June 2026).

Nan, F., Zeng, C., Shen, H. & Lin, L. (2025) ‘Calibration of Integrated Low-Cost Environmental Sensors for Urban Air Temperature Based on Machine Learning’, *Sensors*, 25(11), p. 3398.

Nicholson, S.E. (1988) ‘Land surface atmosphere interaction: Physical processes and surface changes and their impact’, *Progress in Physical Geography*, 12(1), pp. 36–65.

Nuruzzaman, M. (2015) ‘Urban heat island: causes, effects and mitigation measures-a review’, *International Journal of Environmental Monitoring and Analysis*, 3(2), pp. 67–73.

Pan, X., Mavrokapnidis, D., Ly, H.T., Mohammadi, N. & Taylor, J.E. (2024) ‘Assessing and forecasting collective urban heat exposure with smart city digital twins’, *Scientific reports*, 14(1), p. 9653.

Pedregosa, F., Varoquaux, G., Gramfort, A., Michel, V., Thirion, B., Grisel, O., Blondel, M., Prettenhofer, P., Weiss, R., Dubourg, V., Vanderplas, J., Passos, A., Cournapeau, D., Brucher, M., Perrot, M. & Duchesnay, É. (2011) ‘Scikit-learn: Machine Learning in Python’, *Journal of Machine Learning Research*, 12(85), pp. 2825–2830.

Piano, E., De Wolf, K., Bona, F., Bonte, D., Bowler, D.E., Isaia, M., Lens, L., Merckx, T., Mertens, D. & Van Kerckvoorde, M. (2017) ‘Urbanization drives community shifts towards thermophilic and dispersive species at local and landscape scales’, *Global Change Biology*, 23(7), pp. 2554–2564.

Roth, M., Sanchez, B., Li, R. & Velasco, E. (2022) ‘Spatial and temporal characteristics of near-surface air temperature across local climate zones in a tropical city’, *International Journal of Climatology*, 42(16), pp. 9730–9752.

Savu, A. (2025) ‘Temperature highs, climate change salience, and Eco-anxiety: early evidence from the 2022 United Kingdom heatwave’, *Applied Economics Letters*, 32(1), pp. 87–94.

Schinasi, L.H., Benmarhnia, T. & De Roos, A.J. (2018) ‘Modification of the association between high ambient temperature and health by urban microclimate indicators: A systematic review and meta-analysis’, *Environmental Research*, 161pp. 168–180.

Shreevastava, A., Prasanth, S., Ramamurthy, P. & Rao, P.S.C. (2021) 'Scale-dependent response of the urban heat island to the European heatwave of 2018', *Environmental research letters*, 16(10), p. 104021.

Simpson, C.H., Brousse, O. & Heaviside, C. (2024) 'Estimated mortality attributable to the urban heat island during the record-breaking 2022 heatwave in London', *Environmental research letters: ERL [Web site]*, 19(9), p. 094047.

Tran, D.X., Pla, F., Latorre-Carmona, P., Myint, S.W., Caetano, M. & Kieu, H.V. (2017) 'Characterizing the relationship between land use land cover change and land surface temperature', *ISPRS Journal of Photogrammetry and Remote Sensing*, 124pp. 119–132.

Yang, J., Zhou, J., Jiang, J. & Liu, Q. (2025) 'Design of an air temperature sensor using CFD and neural network-based error correction', *IEEE Sensors Journal*,

Yang, X., Zhao, L., Bruse, M. & Meng, Q. (2013) 'Evaluation of a microclimate model for predicting the thermal behavior of different ground surfaces', *Building and Environment*, 60pp. 93–104.

Yi, C., Kwon, H.-G. & Yang, H. (2022) 'Spatial temperature differences in local climate zones of Seoul metropolitan area during a heatwave', *Urban Climate*, 41p. 101012.

Yule, E.L., Hegerl, G., Schurer, A. & Hawkins, E. (2023) 'Using early extremes to place the 2022 UK heat waves into historical context', *Atmospheric Science Letters*, 24(7), p. e1159.